Damage accumulation and cyclic fatigue in Mg-PSZ at Hertzian contacts

Antonia Pajares,[a] Lanhua Wei,[b] and Brian R. Lawn
Materials Science and Engineering Laboratory, National Institute of Standards and Technology, Gaithersburg, Maryland 20899

David B. Marshall
Rockwell International Science Center, 1049 Camino Dos Rios, Thousand Oaks, California 91360

Hertzian contact damage in as-fired, peak-aged, and over-aged Mg-PSZ is studied, in single-cycle and multiple-cycle loading. Indentation stress-strain curves reveal a monotonically increasing quasi-plasticity component in the contact deformation with increasing aging time. A bonded-interface technique is used to obtain surface and subsurface views of the damage zones beneath the spherical indenter. Analytical techniques, including optical and scanning electron microscopy, acoustic emission, Raman spectroscopy, and thermal wave imaging, are used to characterize the damage. The damage patterns are fundamentally different in the three aging states: microfracture-dominated in as-fired; tetragonal-monoclinic phase-transformation-dominated in peak-aged; monoclinic-phase twinning-dominated in over-aged. The damage accumulates with increasing number of cycles, most strongly in the as-fired state. It also increases with increasing test duration in the as-fired and over-aged states, but not perceptibly in the peak-aged. The results imply predominantly mechanical fatigue effects, augmented by a chemical component in the as-fired and over-aged states. Broader implications in relation to the susceptibilities of zirconia ceramics to fatigue degradation in concentrated stress configurations, with special relevance to the evolution of flaws at the microstructural level, are considered.

I. INTRODUCTION

Zirconia-based ceramics can be tailored with uncommonly high long-crack toughnesses and strong R-curves.[1-3] Most widely studied is magnesia-partially-stabilized zirconia (Mg-PSZ), where toughening is due primarily to tetragonal-monoclinic transformation of precipitates within a constraining cubic-phase matrix.[1,2] These zirconia ceramics are subject to fatigue in tests with traditional long-crack (compact tension) specimens.[4,5] Crack extensions in cyclic loading are typically several orders of magnitude higher than in corresponding static loading, indicating a true mechanical fatigue effect, although rate effects from environmental moisture are also in evidence. The growth rates depend on the aging time, declining from the initial (as-fired) state up to a critical aging time (peak-aged), and thereafter increasing (over-aged). This trend correlates with the long-crack toughness values, governed in turn by the extent of tetragonal-monoclinic transformation within the crack-tip shielding zone.[2,3] However, while the role of transformation in the toughening process appears well understood, the underlying mechanisms of fatigue are only recently being elucidated.[4,6,7]

A shortcoming of long-crack tests is the restriction in their capacity for extrapolation down to the scale of the microstructure, where properties like strength and wear are determined. Limited fatigue tests on zirconia specimens containing Vickers radial cracks[8] or naturally occurring surface flaws[9] reveal a dominant influence of local internal forces on the crack growth response in the short-crack region. Insufficient attention has been given to this critical region in the fatigue testing of ceramics.

Here we report on damage and fatigue in a eutectoid-aged Mg-PSZ in the as-fired, peak-aged, and over-aged states using a simple Hertzian test methodology, using a spherical indenter. The Hertzian test has been used to demonstrate the nature and degree of single-cycle and multiple-cycle damage in several other heterogeneous ceramics.[10-18] In those other heterogeneous materials the damage takes the form of distributed discrete deformation events in a confining zone of high compression-shear beneath the contact circle. Such distributed damage zones represent an essential departure from the well-developed tensile cone fractures characteristic of

[a]Guest Scientist, from Departamento de Física, Universidad de Extremadura, 06071-Badajoz, Spain.
[b]Guest Scientist, from Department of Physics and Astronomy, Wayne State University, Detroit, Michigan 48201.

homogeneous brittle materials like glasses, single crystals, and ultra-fine-grain polycrystalline ceramics.[19–22] Preliminary observation of similar distributed damage zones in eutectoid-aged Mg-PSZ have been reported in an earlier communication.[23] In that the damage events within these zones are localized at the microstructural level, the Hertzian test is particularly relevant to the basic issues of flaw evolution in strength determination and material removal in wear. It is also directly pertinent to potential lifetime considerations in engineering contact applications (ball milling, bearings, rollers, dies, etc.) where zirconia ceramics are commonly used.

Accordingly, Hertzian contact damage in Mg-PSZ is analyzed using a variety of complementary characterization techniques: acoustic emission, optical and scanning electron microscopy, Raman spectroscopy, and thermal wave analysis. These techniques reveal the mechanisms of accumulative damage to be fundamentally different in the three aging states: microcracking-dominated in as-fired; tetragonal-monoclinic phase-transformation-dominated in peak-aged; monoclinic-phase twinning-dominated in over-aged. A significant fatigue effect is evident in multiple-cycle loading, most strongly in the as-fired state. The damage accumulates with increasing number of cycles in all states, and with decreasing frequency in the as-fired and over-aged states. These results indicate that the fatigue is largely mechanical in the peak-aged state, but that some additional chemical influence is operative in the other states.

II. EXPERIMENTAL

A. Materials

Eutectoid-aged 9.9 mol % Mg-PSZ (ICI Advanced Ceramics, Australia), as previously described,[5,23] was used in this study. The starting powders were sintered at ≈ 1700 °C, followed by cooling at ≈ 500 °C/h, resulting in an as-fired (AF) material with finely dispersed intergranular lenticular tetragonal (t) precipitates ≈ 100 nm in length within a cubic (c) matrix phase. For this sintering cycle, the precipitates were all well below the critical size for transformation to the monoclinic (m) phase, with $c/t/m$ ratio $\approx 80/20/0$; this provided a convenient baseline material with single-valued toughness ≈ 2 MPa $\cdot$ m$^{1/2}$ (compact tension[5]). Heat treatments at the eutectoid temperature of 1400 °C were then carried out on some specimens to coarsen the precipitates. Such treatment for 2 h produced peak-aged (PA) material with near-critical precipitates ≈ 300 nm and $c/t/m$ ratio $\approx 55/45/0$; this material showed a modest R-curve with long-crack toughness ≈ 6 MPa $\cdot$ m$^{1/2}$. Treatment for 16 h produced over-aged (OA) material with supercritical precipitates ≈ 500 nm and $c/t/m$ ratio $\approx 50/10/40$; for this material, the long-crack toughness declined again, to ≈ 2 MPa $\cdot$ m$^{1/2}$. The grain size of the zirconia materials remained unchanged at ≈ 35 μm throughout the aging process.

B. Indentation tests

Indentation stress-strain curves[10,14,24–26] were measured for each of the zirconia states. Slab specimens 3 mm thick were polished to 1 μm finish with diamond paste and gold coated. Single-cycle indents were made with tungsten carbide spheres of radius 1.98, 3.18, 4.76, 7.94, and 12.7 mm over a range of peak loads 250 to 3000 N on a universal testing machine (Model 1122, Instron, Canton, MA), in laboratory ambient (humidity 50–60%). Using an optical microscope in Nomarski illumination, the surface contact radius a was determined from the residual impression in the gold coating as a function of P for each given sphere radius r, to obtain indentation stress ($P/\pi a^2$) as a function of indentation strain (a/r).[10,23]

Indentation hardnesses (indentation load/projected contact area) were also obtained for each zirconia state using a Vickers indenter at load 50 N for comparison with the indentation stress values.

Multiple-cycle contact damage tests were made using a servo-hydraulic testing machine (Model 8502, Instron, Canton, MA), again in laboratory ambient. These tests were made on bonded-interface specimens,[12,14] prepared by bonding together two polished half-blocks $20 \times 3 \times 3$ mm at a common interface with thin (<5 μm) cyanoacrylate-based adhesive (Loctite Corp., Newington, CT). The top surfaces of the composite specimens were then ground and polished. Contacts over 1 to 10^6 cycles with fixed sphere radius 3.18 mm were made along the trace of the bonded interface over a load cycle $P = 0$ to 500 N, with sinusoidal waveform at frequency 10 Hz. The peak load in this series of tests corresponded to a level just beyond the onset of visible damage in the first cycle. Finally, the indented specimen halves were separated by dissolving the adhesive in acetone.

Some comparative tests were made over single cycles, at a fixed peak load 1000 N but with the sinusoidal period adjusted for contact durations 0.1, 10, and 1000 s, to examine rate effects in the damage response.

C. Characterization of contact fatigue damage

1. Acoustic emission

The damage evolution was monitored *in situ* during some of the single-cycle load-unload tests on the universal testing machine using an acoustic emission facility (LOCAN 320, Physical Acoustics, Princeton, NJ). A piezoelectric transducer was mounted with rubber cement onto the specimen top surface, and damage activity recorded as accumulated acoustic energy versus elapsed time at constant crosshead displacement speed.

2. Microscopy

Top half-surface and section subsurface views of the Hertzian contact damage were obtained by post mortem examination of the separated bonded-interface specimens. The specimens were gold-coated before viewing optically in Nomarski interference contrast. Two-beam interferographs were also taken of some of the indentations, to measure surface depression/uplift associated with the damage zone.

Scanning electron microscopy (SEM) was used to investigate the subsurface damage zones at higher magnification.

3. Raman spectroscopy

The extent of t-m transformation in the AF, PA, and OA subsurface damage zones was analyzed by Raman microprobe spectroscopy.[27] The Raman microprobe spot size was 25 μm, with a lateral and depth resolution of $\approx$20 μm. In one mode of operation, full Raman spectra were measured at the center of the damage zone. These spectra covered the range 10.0 to 30.0 mm^{-1}, with a distinctive monoclinic doublet at 17.8 and 18.8 mm^{-1} and tetragonal peaks at 14.6 and 26.4 mm^{-1}. After subtracting a linear background for each peak the fraction F_m of m-phase relative to the combined $m + t$ content $F_m + F_t = 1$ was calculated using the approximate linear intensity relation[28]:

$$F_m = (I_m^{17.8} + I_m^{18.8})/[(I_m^{17.8} + I_m^{18.8}) + (I_t^{14.6} + I_t^{26.4})] \quad (1)$$

In another operative mode, the Raman shift was fixed at the monoclinic peak 17.8 mm^{-1} or tetragonal peak 14.6 mm^{-1}, and the probe scanned along a prescribed line through the damage zone.

4. Thermal wave analysis

Thermal wave imaging was used to obtain images of the damage zones and estimates of microcrack densities.[17,29] Sections of indented, gold-coated specimen surfaces were irradiated with a chopped argon-ion laser heating beam, over a spot of size $\approx$20 μm diameter, and scanned with a helium-neon laser probe beam at grazing incidence.[30] The intermittent heating produces periodic thermal waves in the underlying material. The diffusion of these waves away from the central spot is sensitive to the microcrack content in the heated volume. Consequent variations in the specimen near-surface heating conditions are monitored by a detector which locates deflections of the refracted probe beam. Measurement of the deflections enables relative evaluation of the local thermal diffusivity, α/α_O, where α is the diffusivity inside the damage zone and α_O outside. This diffusivity represents an average value over a specimen volume

determined by a thermal-wave wavelength, $\approx$100 μm in our experiments. With this evaluation one may evaluate the microcrack density using the Hasselman relation[31]

$$Nc^3 = \beta(\alpha_O/\alpha - 1) \quad (2)$$

where N is the microcrack volume density, c is a characteristic crack dimension, and the coefficient $\beta = 9/8$ for randomly oriented penny cracks.

The experiment was also operated in a scanning mode, in which the laser heating and probe beams were held fixed and the specimen was rastered via a stepping motor to generate thermal wave images of the damage zones.[30]

III. RESULTS

A. Indentation stress-strain curves

Figure 1 shows indentation stress-strain curves for single-cycle indentations in AF, PA, and OA Mg-PSZ. The inclined dashed line is the reference Hertzian relation $p_0 = (3E/4\pi k)a/r$ for purely elastic contacts,[10] using Young's modulus $E = 210$ GPa for Mg-PSZ and coefficient $k = 0.69$ for WC spheres on Mg-PSZ.[23] The solid curves through the data are empirical fits. The curves bend over more strongly with heat-treatment time, i.e., in the order AF $\rightarrow$ PA $\rightarrow$ OA, indicating increasing quasi-plasticity with increasing precipitate size.

Hardness numbers from Vickers indentations are included as the horizontal dashed lines at upper right
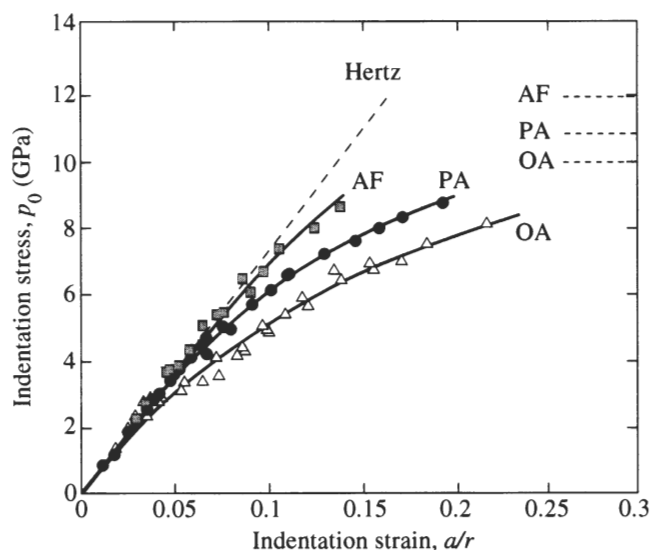

FIG. 1. Indentation stress-strain curves for eutectoid-aged Mg-PSZ, using WC spheres of radius 1.98, 3.18, 4.76, 7.94, and 12.70 mm (not distinguished on data points). Data for as-fired (AF), peak-aged (PA), and over-aged (OA) states. Solid curves are empirical fits to the data. Inclined dashed line is calculated Hertzian linear elastic response for WC sphere on Mg-PSZ. Horizontal dashed lines at upper right are Vickers hardness values.

in Fig. 1. These numbers serve to confirm the trend shown by the spherical indentations toward increasing deformation with increasing heat-treatment time.

B. Acoustic emission

Figure 2 shows plots of cumulative acoustic energy as a function of loading time for Hertzian indentation cycles in AF, PA, and OA Mg-PSZ at sphere radius 3.18 mm and peak load 1500 N. The acoustic activity is relatively intense in AF, modest in OA, and barely detectable in PA. Note that this order does not correlate with the trend shown by the stress-strain curves in Fig. 1; and that the most active state, AF, is also the least nonlinear in Fig. 1.

In all three states the acoustic activity occurs predominantly during the loading half-cycle. This activity is attributed to microcrack *initiation*.[23] Note that this does not preclude the possibility that the microcracks undergo the bulk of their *propagation* during *un*loading, upon removal of a highly stabilizing compressive elastic component of the Hertzian field.[32]

C. Microscopy

1. Single-cycle damage

First consider single-cycle contact damage. Figure 3 shows surface views of indentations in AF, PA, and OA Mg-PSZ made at sphere radius 3.18 mm and peak load 1500 N (corresponding to indentation pressures p_0 well beyond the elastic limit—cf. Fig. 1), in Nomarski contrast (left) and two-beam interference (right):

(i) AF ($p_0 = 6.3$ GPa). The Nomarski contrast micrograph reveals surface traces of incipient cone cracks at the contact periphery. The interferograph

fringe displacements indicate a small residual depression (< 0.11 μm) over the contact diameter (≈ 550 μm) relative to the far-surface level, corresponding to a near-elastic contact. There is minor uplift outside the contact.

(ii) PA ($p_0 = 5.5$ GPa). The residual impression is smoothly depressed within the contact, without surrounding ring cracks but with traces of peripheral discrete damage. These peripheral damage traces tend to align at $\approx 45°$ to the radial and hoop directions,[33] along the shear trajectories. Analogous traces around Vickers indentations have been identified with phase transformation in transmission electron microscopy studies.[34] The impression depth measured from the interferograph (0.35 μm) is well in excess of that in AF, consistent with the trend to increased quasi-plasticity in Fig. 1. Outside the impression edge there is substantial uplift.

(iii) OA ($p_0 = 4.9$ GPa). The contact depression is even more evident, without peripheral damage but with a recurrence of incipient cone cracks. From the interferograph the impression depth is 1.76 μm, greater than in PA, again consistent with the trend to increased deformation in Fig. 1. In this instance there is no indication of any surface uplift outside the contact.

Figure 4 shows bonded-interface section views of contact damage in each of the material states, for a load sequence 250, 500, 1000 N, sphere radius 3.18 mm. A progressive increase in extent of damage with load is evident in each state. In no case, not even in AF and OA, is there any sign of downward penetration of the ring cracks previously evident in Fig. 3. Instead, the deformation assumes the form of discretely distributed damage within a confined quasi-plastic subsurface zone. Notwithstanding macroscopic similarities in these subsurface zones in the three material states, indicative of a common compression–shear driving force,[10,14] there are some essential differences in the nature of the underlying damage mechanisms:

(i) AF. The region beneath the contact reveals microcracks. These appear to be intergranular, indicative of weak grain boundaries. At load 250 N there is barely any indication of damage. A few isolated microcracks are observed at 250 N, and these are confined beneath the contact surface, in the region of maximum shear stress.[10,14,17] The section area and density of microcracks increase with load until, at 1000 N, the microcracks appear to have coalesced into a network pattern, and some grain pullouts are evident. The high density of microcracks in this last case is consistent with the strong acoustic emission for AF in Fig. 2.

(ii) PA. No microcracks are evident at any of the loads. Instead, the subsurface damage is characterized by a distinctive surface rumpling,[34–36] again with some slight tendency for the deformation to align along shear trajectories[33,34] (cf. PA in Fig. 3). It is evident from
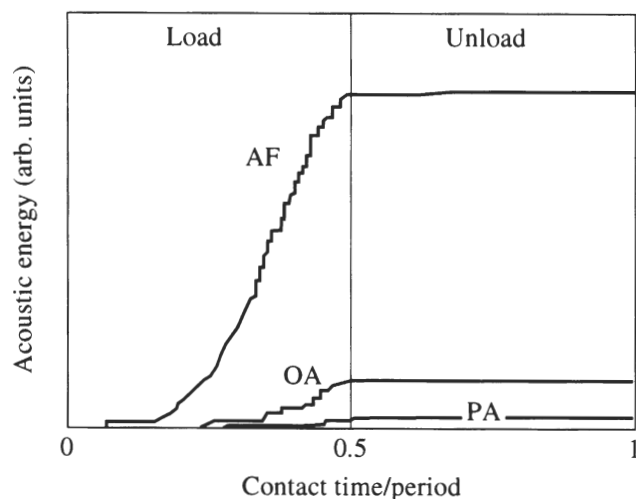
FIG. 2. Cumulative acoustic energy versus normalized contact time during load-unload indentation cycle at constant crosshead speed in AF, PA, and OA Mg-PSZ specimens, using WC sphere of radius 3.18 mm at peak load 1500 N.
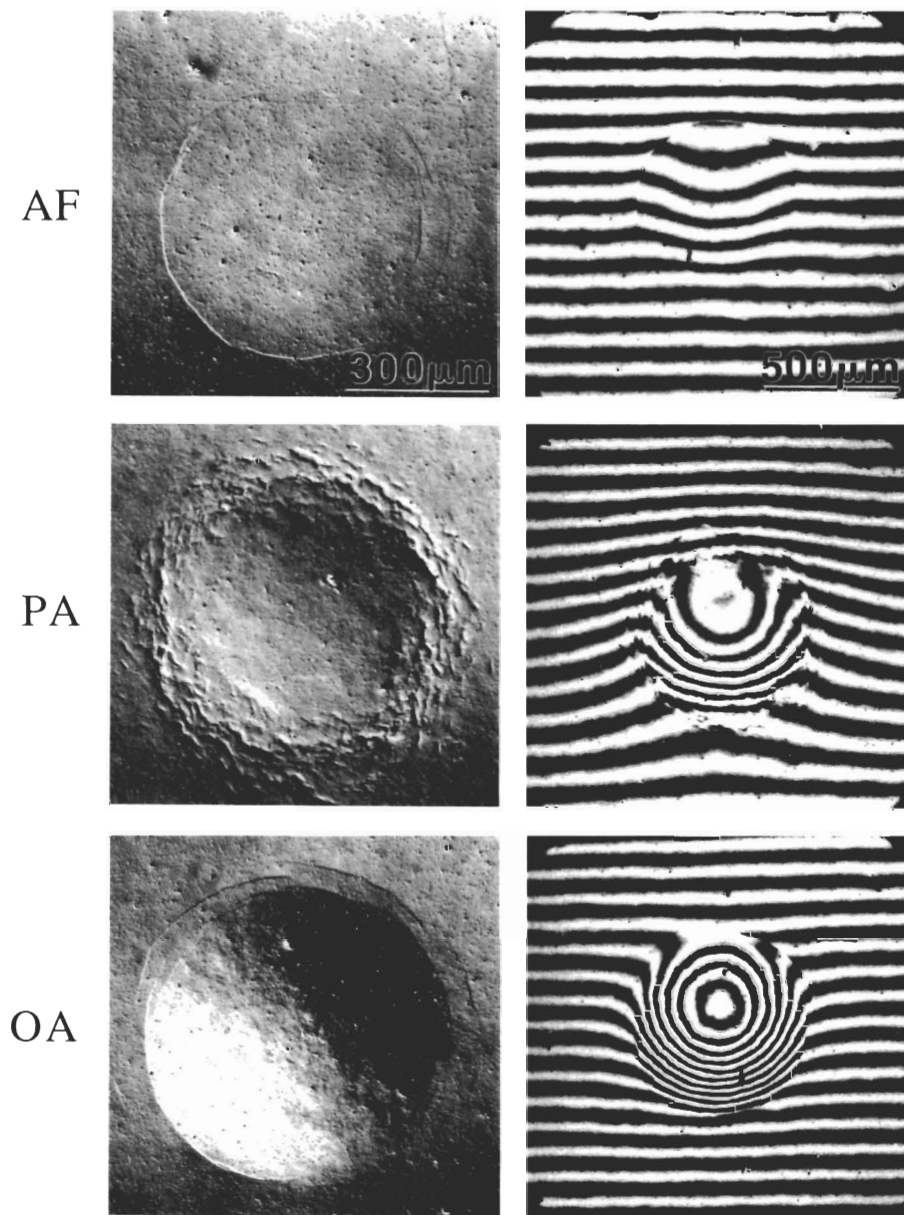
FIG. 3. Surface views of single-cycle Hertzian damage in AF, PA, and OA Mg-PSZ, made with WC sphere of radius 3.18 mm at peak load 1500 N. Nomarski interference at left. Two-beam interference at right; each fringe spacing indicates surface change of one half wavelength λ ($\lambda = 0.54$ μm). (Note different scales at left and right.)

the stress-strain curves in Fig. 1 and the two-beam interferographs in Fig. 3 that phase transformation in PA is more effective than microcracking in AF as a mode of nonlinear deformation.

(iii) OA. The damage is less well defined in comparison to the other states. There is some surface rumpling, but not to the extent seen in PA, and with no alignment along shear trajectories. There are microcracks along grain boundaries, but not to the extent seen in AF, once more consistent with the acoustic emission data in Fig. 2. Yet the degree of quasi-plastic deformation (Figs. 1 and 3) is higher in OA than in both AF and PA. The

indications are of an altogether different, more potent mode of contact deformation in this last material state.

2. Multiple-cycle damage

Now consider multiple-contact damage. Nomarski micrographs in Fig. 5 show subsurface damage in AF, PA, and OA Mg-PSZ with increasing number of cycles $n = 1$, 10^2, 10^4, and 10^6, for contacts at intermediate load 500 N (cf. Fig. 4), sphere radius 3.18 mm, frequency 10 Hz. In each material state the damage zones expand progressively in size and density with n:
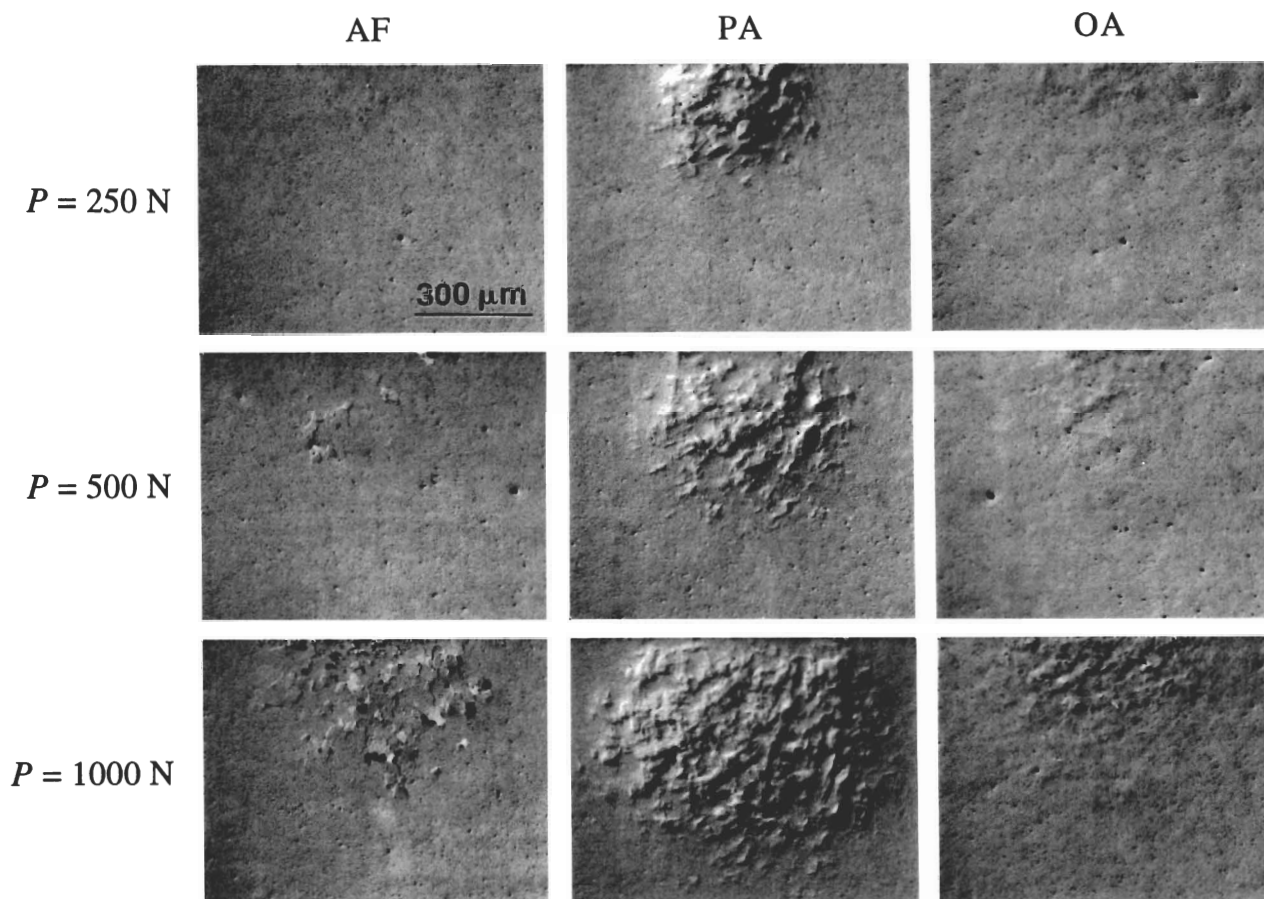
FIG. 4. Subsurface views of single-cycle Hertzian damage in AF, PA, and OA Mg-PSZ, made with WC sphere of radius 3.18 mm at peak load 250 N, 500 N, and 1000 N, cycle duration 10^3 s. Sections obtained using bonded–interface section technique.

(i) AF. Microcrack damage increases progressively with n, with an end result after 10^6 cycles at this contact load comparable to that after a single cycle at twice the load (cf. Fig. 4).

(ii) PA. The degree of surface rumpling increases with n. After 10^6 cycles isolated microcracks have opened up along the grain boundaries, indicating a strong buildup of residual stresses within the transformation zone.

(iii) OA. Again, the microcrack density and surface rumpling increase with n, although never to the respective levels observed in AF and PA.

Higher magnification SEM views of the central damage zones are shown in Fig. 6 for each of the materials, for the indentations at 10^6 cycles in Fig. 5. Some microcracking is observed in each of the materials, most strongly in AF, with relatively clean intergranular cracks and grain ejections.

Figure 7 shows damage for single-cycle contact at different test durations in the three materials. These tests show that the density of microcracks and the size of the damage zone increase markedly at longer durations in the

AF material. The increase in damage is comparatively modest in the OA, and almost imperceptible in the PA.

D. Raman spectroscopy

Raman spectroscopic data for AF, PA, and OA Mg-PSZ from single-cycle subsurface damage zones are shown in Figs. 8 and 9, for indentations at sphere radius 3.18 mm and load 1000 N. Figure 8 shows variations in intensity of the m-phase peak at fixed wave number 17.8 mm^{-1} and t-phase peak at fixed wave number 14.6 mm^{-1} along linear traces parallel to the top surface at depth 250 μm through the damage zones (inset). It is clear that the degree of indentation-generated t-m transformation is insignificant in the AF and OA states, but substantial in PA.

Figure 9 shows full spectra from stationary spots within (heavy curves) and without (light curves) the damage zones (inset), normalized relative to the intensity at Raman shift 10 mm^{-1} (left axis), and with the background removed, for each of the states. Note the near-coincidence of heavy and light curves in both AF
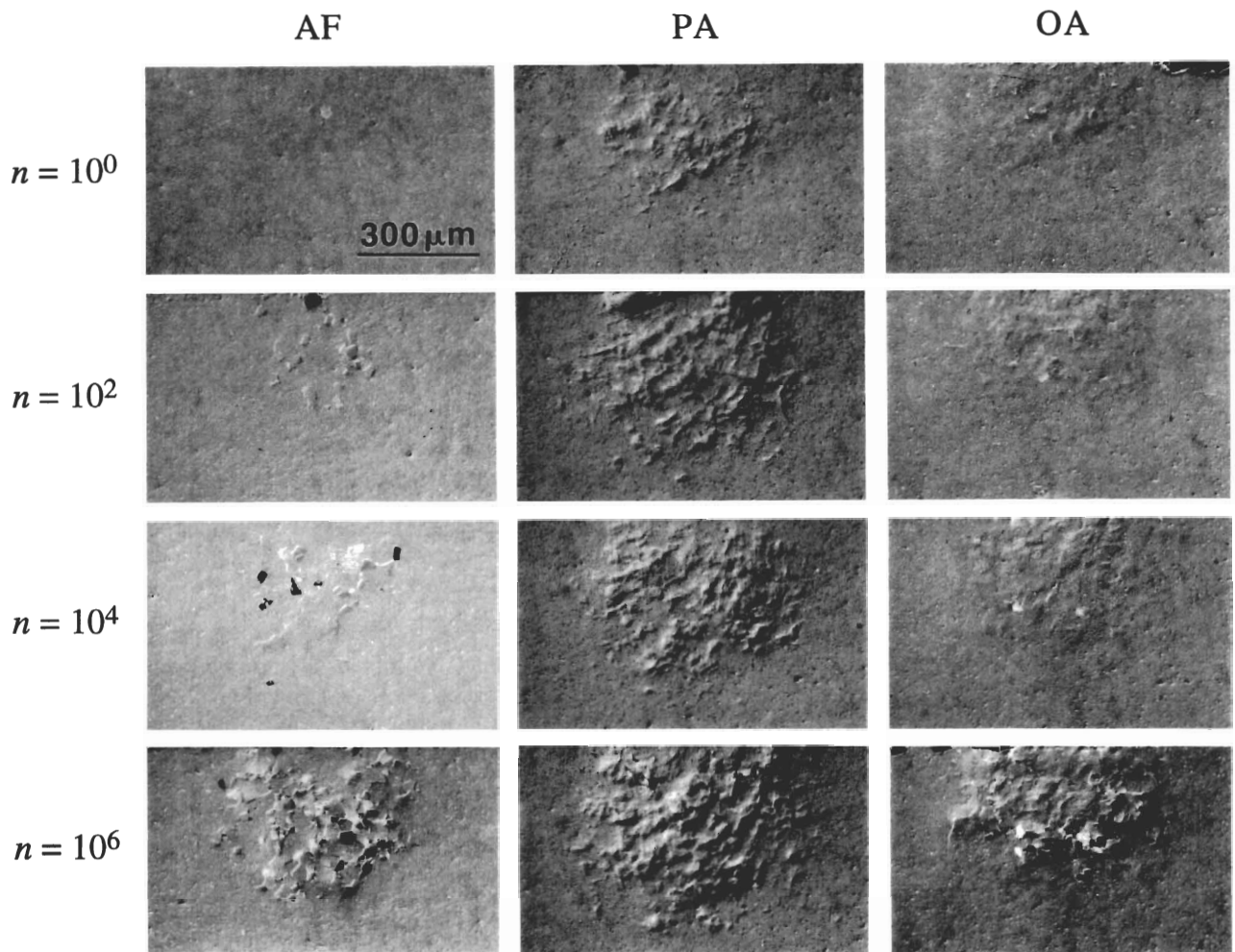
FIG. 5. Subsurface views of multiple–cycle Hertzian damage in AF, PA, and OA Mg–PSZ, made with WC sphere of radius 3.18 mm at peak load 500 N. Tests for specified number of cycles n, at frequency 10 Hz. Sections obtained using bonded-interface section technique.

and OA, indicating virtually no phase transformation in those states. In PA, on the other hand, there is a significant shift from t-phase to m-phase within the damage zone, consistent with Fig. 8. Such data allow quantitative evaluations of the m-phase fraction F_m from Eq. (1). For AF and OA, the m-phase concentration remains the same inside the damage zone as outside, at $F_m \approx 0$ and 1, respectively. In PA, however we find a significant increase in the m-phase content, from $F_m \approx 0$ without to $F_m \approx 0.23$ within.

Comparative spectra after cycling for 10^6 cycles at frequency 10 Hz show further significant peak shifts in the PA material, but again not in AF and OA. The fatigue effect in PA is illustrated in Fig. 10, with a comparative point-by-point plot of F_m as a function of depth along a subsurface centerline through damage sections at $n = 1$ and 10^6:

(i) The fatigue is substantial: the maximum value of F_m after 10^6 cycles is about twice that after first contact.

This increase in damage intensity with n correlates with the progressive buildup of subsurface damage evident in the PA micrographs in Fig. 5.

(ii) At each n, there is a rapid initial increase in F_m to a maximum at depth ≈ 100 μm. Thereafter, the relative fraction of m-phase decreases monotonically, ultimately saturating at the background level at depth 400–600 μm. The relative low values of F_m at the top surface are consistent with a lack of visible surface rumpling immediately below the PA specimen surface in Figs. 4 and 5.

(iii) The t-m transformation is only *partial*; i.e., F_m does not exceed 0.2 at any point of the damage zone.

Similar traces in PA after a single cycle at test durations 10^{-1}, 10, and 10^3 s show no significant load rate variation (cf. PA in Fig. 7).

Thus, the role of phase transformation in the damage accumulation, especially as it relates to fatigue, is important in PA, but not in the other states.
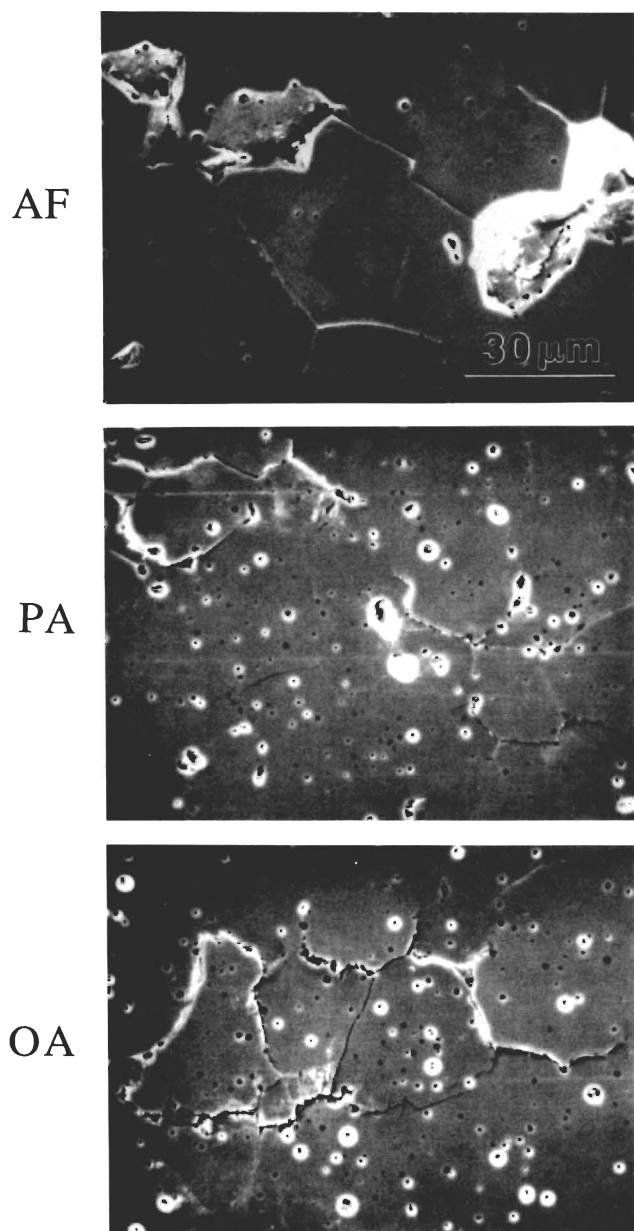
FIG. 6. Scanning electron micrographs of multiple-cycle Hertzian damage in AF, PA, and OA Mg-PSZ, after 10^6 cycles in Fig. 5.

E. Thermal wave

Thermal wave images of the subsurface damage patterns in each of the materials after 10^5 cycles at 1000 N are shown at the right in Fig. 11. These images may be compared with the corresponding Nomarski micrographs at the left. Thermal waves are sensitive only to the microfracture damage, and not to phase transformation or other deformation modes which produce defect structures with closed interfaces.[17] Thus we observe relatively high microfracture contrast in AF, modest in OA, and virtually nothing in PA, consistent with the acoustic emission data in Fig. 2. For PA, the singular non-correspondence between the thermal wave and Nomarski images is strong confirmation of a damage mode other than microfracture.

Quantitative evaluations of subsurface microcrack densities for AF, PA, OA Mg-PSZ in Fig. 5 using Eq. (2), after $n = 1$, 10^2, 10^4, and 10^6 indentations at load 500 N and frequency 10 Hz, are shown in Fig. 12. A marked increase in the damage accumulation is evident as the number of cycles builds up, most noticeably in AF but also to a limited extent in OA. Similar strong damage buildup has been reported in heterogeneous silicon carbides with weak interphase boundaries.[18] Note that the microcrack density in PA remains near-zero up to $n = 10^6$, despite the occasional observation of individual microcracks in Figs. 5 and 6, indicating that the density is below the threshold of detection.

IV. DISCUSSION

A. Single-cycle damage

The observations of Hertzian contact damage in the as-fired, peak-aged, and over-aged Mg-PSZ presented in the previous sections reveal macroscopically similar quasi-ductile deformation processes, all driven by the same shear component of the contact field but each different in its underlying microscopic source. We consider each state in turn, starting with the peak-aged, optimally toughened state, focusing first on single-cycle damage:

(i) PA. Despite its optimal toughness, the peak-aged state shows an intermediate stress-strain response in Fig. 1 and surface impression depth in Fig. 3; i.e., more compliant than AF, but less than OA. The section views in Figs. 4, 5, and 7 reveal considerable surface rumpling within the damage zone, with some alignment along shear trajectories, indicative of t-m phase transformations.[2,34,35] The Raman data in Figs. 8 and 9 confirm the transformation mode. Note that the hydrostatic component of Hertzian stress within the damage zone is compressive,[10,14,32] not tensile as is the case around propagating crack tips, so in this instance it is solely the shear component that is responsible for triggering the transformation. Note also from Fig. 10 that the maximum density of transformed precipitates occurs at a depth $\approx 100~\mu m$ below the indented surface, corresponding to ≈ 0.5 contact radius, where the Hertzian shear stresses are maximum (cf. 500 N indents in Fig. 4). Notwithstanding this dominance of shear as the active stress, the transformation is highly dilatant, which would account for the large surface uplift outside the PA indentations in Fig. 3.

No significant cracking of any kind in the PA material is manifest in the optical micrographs, nor in the acoustic emission data in Fig. 2 or thermal wave data in Fig. 12, presumably because of the extra compression
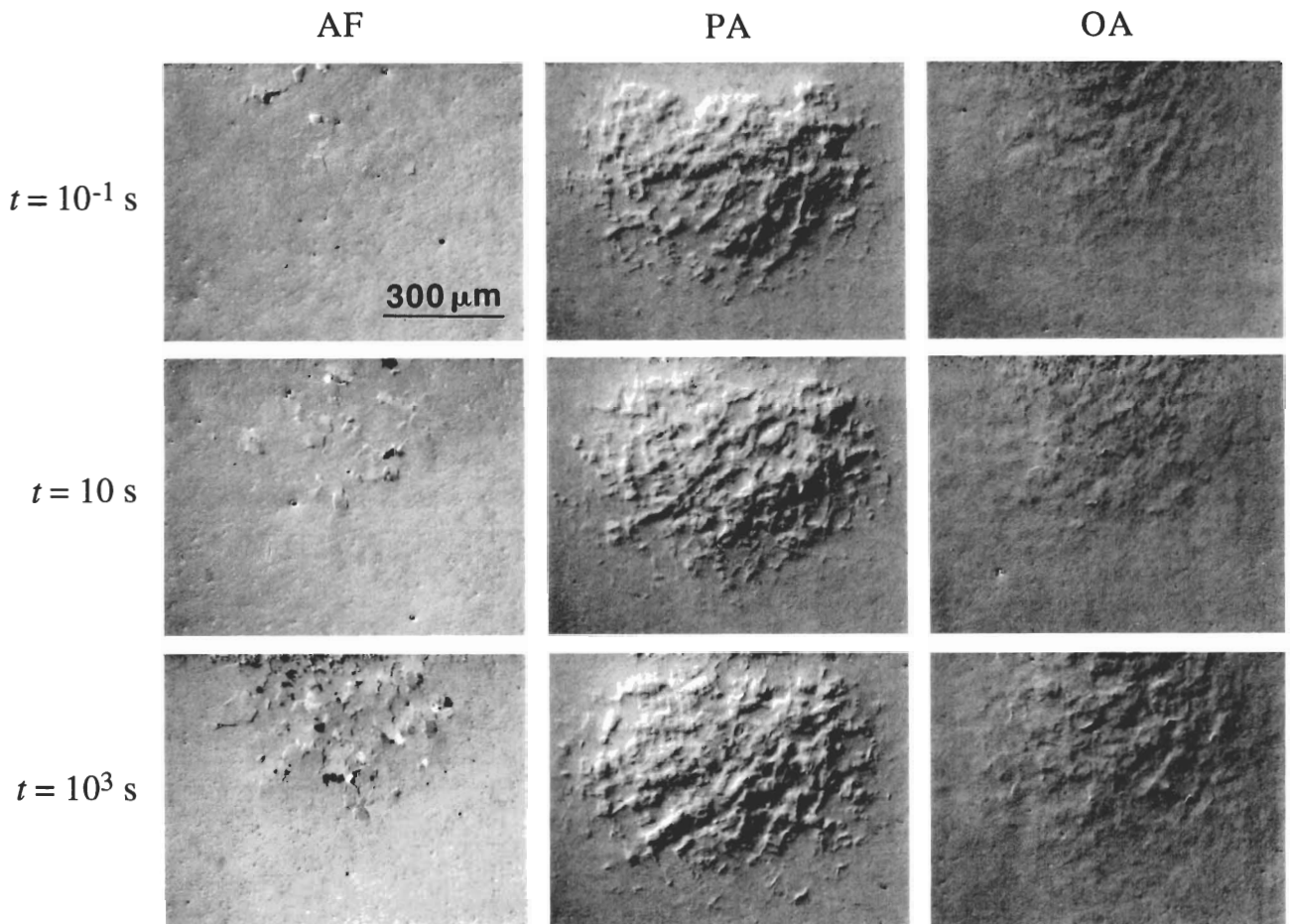
FIG. 7. Subsurface views of single-cycle Hertzian damage in AF, PA, and OA Mg-PSZ, made with WC sphere of radius 3.18 mm at peak load 1000 N. Tests for test durations 10^{-1}, 10, and 10^3 s. Sections obtained using bonded-interface section technique.

from the transformations. It is only after the most severe cycling that the first signs of microcracking become evident, in the SEM micrographs in Fig. 6.

(ii) AF. The as-fired material shows no sign of any phase transformation in the micrographs of Figs. 4, 5, and 7 or in the Raman data in Figs. 8 and 9. This is consistent with the near-elastic stress-strain curve in Fig. 1, and comparatively small contact depression in Fig. 3. On the other hand, distributed subsurface facet-scale grain boundary microcracks are apparent in the subsurface damage zone. The acoustic emission data in Fig. 2 and thermal wave data in Figs. 11 and 12 show that the density of these microcracks is relatively high in AF (although not so high as to increase the local compliance substantially in Fig. 1). Close inspection of the optical (Figs. 4, 5, and 7) and SEM (Fig. 6) micrographs provides no indication of any intragranular shear faults (e.g., twins, crystallographic slip planes). Such faults are a vital precursor to intergranular microcrack imitation in some brittle solids with moderately weak boundaries, as for instance in some aluminas[10] and silicon nitrides.[17]

Instead, the damage appears to involve simple intergranular breakdown, characteristic of structures whose boundaries are so weak as to fail at shear stresses below those for intragranular fault activation; machinable mica-containing glass-ceramics[14,16] and some heterogeneous silicon carbides[11,37] fall into this category. Like phase transformation, microcracking is dilatant, which would contribute to the minor uplift around the AF impression in Fig. 3.

We note the departure from classic fracture behavior for homogeneous brittle materials. Incipient ring cracks are apparent in the AF surface view in Fig. 3, but not in the subsurface views in Figs. 4, 5, and 7. Downward propagation of these ring cracks is suppressed by deflection along weak grain boundary facets, away from the tensile stress trajectories and into a highly compressive stress state.[19] In this context we recall the moderately large grain size in the Mg-PSZ used in the present study, ≈ 35 μm, relative to the scale of the contact radius, ≈ 300 μm (cf. Fig. 3); hence the deflections are significant on the scale of the Hertzian field. As

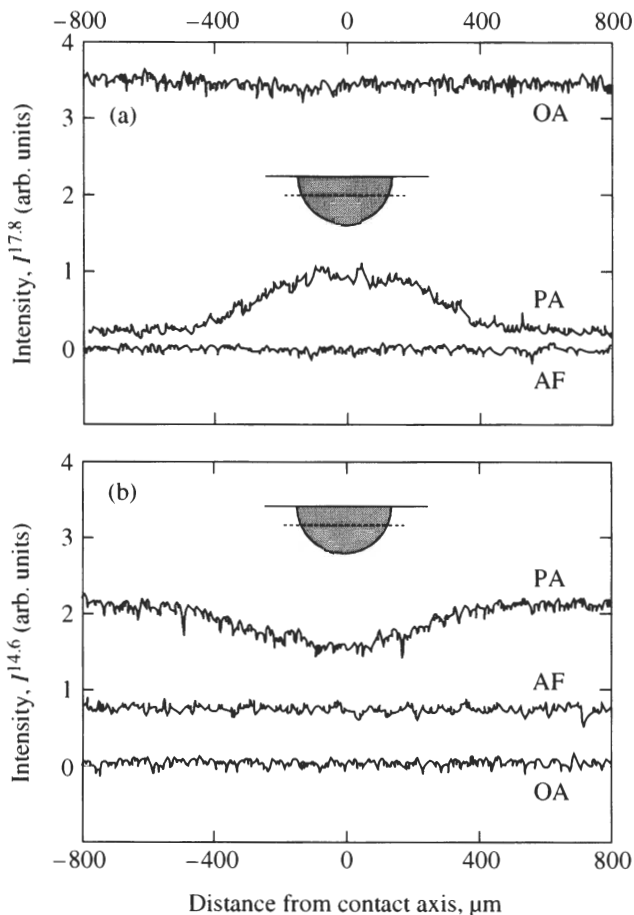FIG. 8. Variation in intensity of Raman-shifted beam along trace at depth 250 μm through subsurface single-cycle Hertzian damage zone (dashed line in inset) in AF, PA, and OA Mg-PSZ. Beam fixed at (a) monoclinic peak 17.8 mm^{-1}, (b) tetragonal peak 14.6 mm^{-1}. Indentations made with WC sphere of radius 3.18 mm at peak load 1000 N.
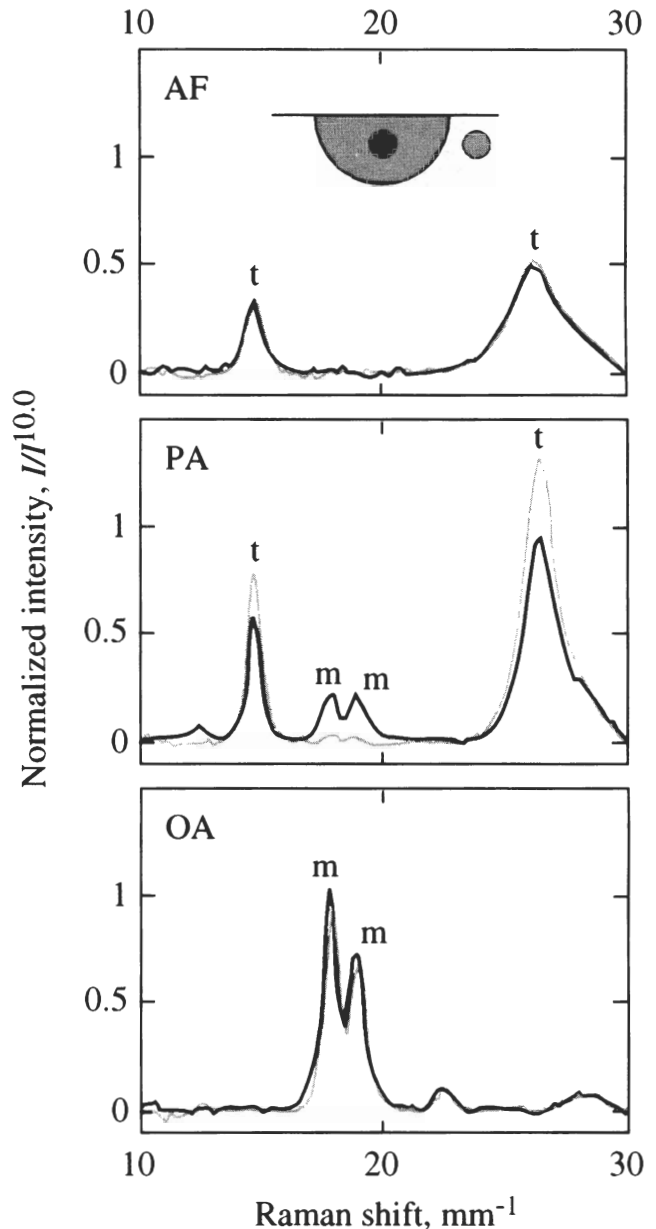

FIG. 9. Raman shift spectra for single-cycle Hertzian subsurface damage zones in AF, PA, and OA Mg-PSZ. Solid heavy curves taken *within* damage zone, light curves *without* (inset). Tetragonal (*t*) and monoclinic (*m*) peaks marked. Intensity normalized relative to level at wave number 10 mm^{-1}, background removed. Indentations made with WC sphere of radius 3.18 mm at peak load 1000 N.

has been documented for alumina,[12] the suppression of cone fracture is dramatically more pronounced at larger grain sizes.

(iii) OA. Again in the over-aged state there is no indication of any phase transformation in the Raman data of Figs. 8 and 9. Yet this state is substantially more compliant than either AF or PA, Fig. 1, with the greatest contact depression, Fig. 3. Some surface rumpling is apparent in the micrographs, Figs. 4, 5, and 7, albeit without the shear trajectory alignment observed in PA. It is evident that some other deformation mechanism, one even more susceptible to shear stress than phase transformation, must exist in the OA state. Previous studies have identified low-stress twinning within transformed monoclinic particles as a principal source of such deformation.[38,39] This implies an altogether different deformation geometry, which could account for the lack of significant uplift around the OA impression in Fig. 3.

As indicated from the micrographs and from the acoustic data (Fig. 2) and thermal wave data (Figs. 11 and 12), some intergranular microcracking accompanies the deformation. However, the microcrack density is modest (Fig. 12) and, as we have seen in the case of AF, is unlikely to make a major contribution to the net deformation. Again, surface ring cracks are apparent (Fig. 3), but never develop into fully fledged cones.
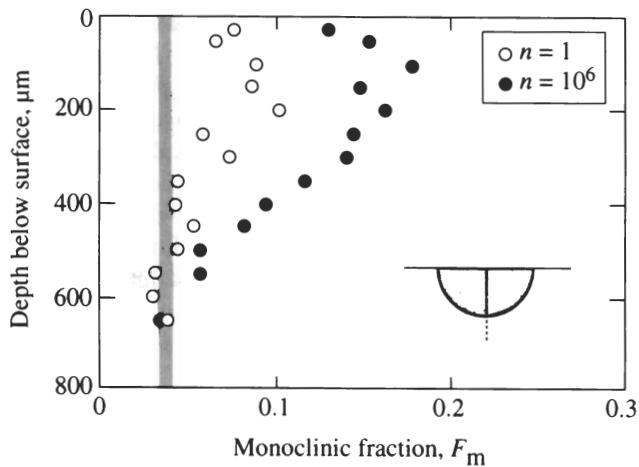
FIG. 10. Variation of monoclinic fraction F_m (relative to total $m + t$ content), evaluated from Raman spectra using Eq. (1) as function of depth along Hertzian subsurface centerline (dashed line in inset). Shaded vertical band is background level of F_m away from damage zone. Indentations at WC sphere radius 3.18 mm, load 500 N after 1 and 10^6 cycles (frequency 10 Hz). Note relative increase in monoclinic fraction after fatigue.

B. Cyclic fatigue

Now consider cyclic fatigue. The contact test provides an alternative approach to that of more traditional long-crack fatigue testing. What can we learn about fatigue mechanisms in zirconia from the present study that is not already known from such more traditional studies? Compact-tension tests on AF, PA, and OA Mg-PSZ show relative K-shifts on velocity $(v - K)$ curves,[4,5,9] consistent with a common intrinsic crack growth mechanism but a change in the level of crack-tip shielding.[40] Tension-compression tests show considerable stress-strain hysteresis, pointing the way to the role of phase transformation and other microstructural processes.[6,7]

In the Hertzian contact tests, we distinguish different modes of damage in each of the three material states: predominantly microcracking in AF, transformation in PA, and (presumed) twinning in OA. The density and spatial extent of each of these damage modes increases conspicuously with number of cycles. These buildups are ultimately attributable to hysteresis in each of the underlying damage events in reversed loading.[41–43] The existence of hysteresis in the martensitic t-m phase transformation is well documented.[2] Hysteresis also oc-
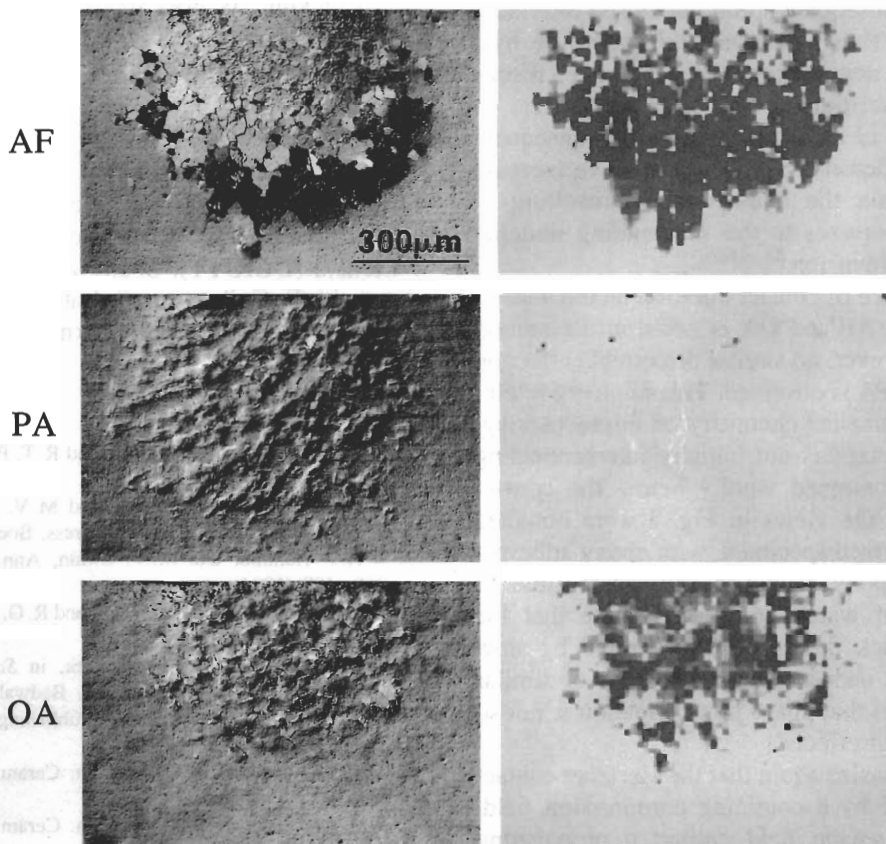

FIG. 11. Comparison of thermal wave images (right) with Nomarski interference micrographs (left). Multiple-cycle Hertzian damage in AF, PA, and OA Mg-PSZ, made with WC sphere of radius 3.18 mm at peak load 1000 N, 10^5 cycles (frequency 10 Hz).
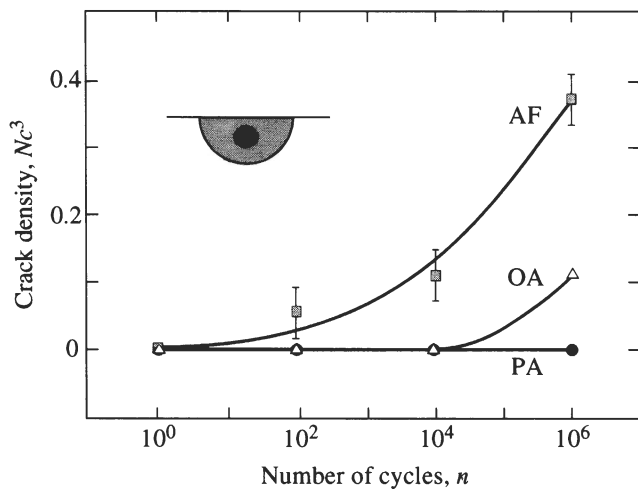
FIG. 12. Microcrack densities at center of subsurface Hertzian damage zone (inset) as function of number of indentation cycles, evaluated using thermal wave determinations of thermal diffusivity in Eq. (2). For indentations from Fig. 5. Solid curves are empirical fits through data. Error bars indicate bounds estimated from point-to-point scatter in thermal wave signal within damage zone (shown only for AF for clarity).

curs at microcracks, specifically from release of thermal expansion stresses upon initial formation and from frictional tractions at subsequent sliding at closed interfaces in shear fields.[32,44] Twinning is also known to be hysteretic. Mechanical degradation, thence fatigue, results from progressive attrition of the internal barriers to reversibility in each of these processes, with consequent buildup in damage density[43]; or, to progressive increase in compliance within the damage zone, resulting in transfer of critical stresses to the surrounding material and thus to zone expansion.[32]

A strong influence of contact duration on the density of microcracking in AF and OA is noted in the section views in Fig. 7; however, no similar discernible effect on the damage zone in PA is observed. This implies a potential effect of environmental chemistry on microcracking, even though the damage is not initially interconnecting and is ostensibly contained wholly below the contact surface. Recall that the views in Fig. 7 were obtained using a bonded-interface specimen, with epoxy adhesive at the interface. Epoxy is notoriously susceptible to the interdiffusion of water, so it is possible that the subsurface microcrack density is exaggerated by slow crack growth at the near-interface. The lack of similar effect in PA indicates that phase transformation is not so sensitive to chemical effects.

We would emphasize again that the Hertzian contact test is characterized by a confining compression field, in contrast to the tensile field around a propagating crack tip. Hence one should be extremely cautious before translating conclusions drawn from observations of indentation damage to long-crack shielding zones; such an implied complementarity can lead to fallacious conclusions concerning crack-tip processes.[45] In the contact field, the compressive component suppresses macroscopic fracture, and promotes instead an altogether different, damage accumulation mode of failure (including discrete microfracture) not evident in traditional long-crack tests. Conversely, of course, long-crack tests can provide little reliable guide to the fatigue response in contact configurations.

C. Implications

The uses of zirconia in many applications involve contact stresses, e.g., bearings, valves, medical implants. The contact tests described here provide insight into the mechanisms of damage and fatigue in the different aging states of Mg-PSZ. In general, the PA state is preferred for most applications because, quite apart from its optimal toughness, any tendency to microcracking is suppressed by the superposed contact and transformation compression fields. Accordingly, PA is least strength-degrading[5] and most wear-resistant [S. Lathabai, unpublished work]. AF is most susceptible to microcracking, and least compliant, and therefore too brittle for most applications. On the other hand, OA, although still susceptible to microcracking, is also most compliant, and therefore has potential use where energy absorption is a primary concern, e.g., thermal shock.

REFERENCES

1. R. C. Garvie, R. H. J. Hannink, and R. T. Pascoe, Nature **258**, 703 (1975).
2. D. J. Green, R. H. J. Hannink, and M. V. Swain, *Transformation Toughening of Ceramics* (CRC Press, Boca Raton, FL, 1989).
3. R. H. J. Hannink and M. V. Swain, Ann. Rev. Mater. Sci. **24**, 359–408 (1994).
4. R. H. Dauskardt, D. B. Marshall, and R. O. Ritchie, J. Am. Ceram. Soc. **73**, 893–903 (1990).
5. S. Lathabai and R. H. J. Hannink, in *Science and Technology of Zirconia V,* edited by S. P. S. Badwal, M. J. Bannister, and R. H. J. Hannink (Technomic Publishing Co., Lancaster, PA, 1993), pp. 360–370.
6. S-Y. Liu and I-W. Chen, J. Am. Ceram. Soc. **75**, 1191–1204 (1992).
7. S-Y. Liu and I-W. Chen, J. Am. Ceram. Soc. **77**, 2025–2035 (1994).
8. S-Y. Liu and I-W. Chen, J. Am. Ceram. Soc. **74**, 1206–1216 (1991).

9. A. A. Steffen, R. H. Dauskardt, and R. O. Ritchie, J. Am. Ceram. Soc. **74**, 1259–1268 (1991).
10. F. Guiberteau, N. P. Padture, H. Cai, and B. R. Lawn, Philos. Mag. A **68**, 1003–1016 (1993).
11. N. P. Padture and B. R. Lawn, J. Am. Ceram. Soc. **77**, 2518–2522 (1994).
12. F. Guiberteau, N. P. Padture, and B. R. Lawn, J. Am. Ceram. Soc. **77**, 1825–1831 (1994).
13. B. R. Lawn, N. P. Padture, H. Cai, and F. Guiberteau, Science **263**, 1114–1116 (1994).
14. H. Cai, M. A. Stevens Kalceff, and B. R. Lawn, J. Mater. Res. **9**, 762–770 (1994).
15. H. Cai, N. P. Padture, B. M. Hooks, and B. R. Lawn, J. Europ. Ceram. Soc. **13**, 149–157 (1994).
16. H. Cai, M. A. S. Kalceff, B. M. Hooks, B. R. Lawn, and K. Chyung, J. Mater. Res. **9**, 2654–2661 (1994).
17. H. H. K. Xu, L. Wei, N. P. Padture, B. R. Lawn, and R. L. Yeckley, J. Mater. Sci. **30**, 869–878 (1995).
18. N. P. Padture and B. R. Lawn, J. Am. Ceram. Soc. **78**, 1431–1438 (1995).
19. F. C. Frank and B. R. Lawn, Proc. R. Soc. London. **A299**, 291–306 (1967).
20. B. R. Lawn and T. R. Wilshaw, J. Mater. Sci. **10**, 1049–1081 (1975).
21. A. G. Evans and T. R. Wilshaw, Acta Metall. **24**, 939–956 (1976).
22. K. Zeng, K. Breder, and D. J. Rowcliffe, Acta Metall. **40**, 2601–2605 (1992).
23. A. Pajares, F. Guiberteau, B. R. Lawn, and S. Lathabai, J. Am. Ceram. Soc. **78**, 1083–1086 (1995).
24. D. Tabor, *Hardness of Metals* (Clarendon, Oxford, 1951).
25. M. V. Swain and B. R. Lawn, Phys. Status Solidi **35**, 909–923 (1969).
26. M. V. Swain and J. T. Hagan, J. Phys. D: Appl. Phys. **9**, 2201–2214 (1976).
27. D. B. Marshall, M. C. Shaw, R. H. Dauskardt, R. O. Ritchie, M. J. Readey, and A. H. Heuer, J. Am. Ceram. Soc. **73**, 2659–2666 (1990).
28. D. R. Clarke and F. Adar, J. Am. Ceram. Soc. **65**, 284–288 (1982).
29. D. T. Smith and L. Wei, J. Am. Ceram. Soc. **78**, 1301–1304 (1995).
30. L. Wei, *Thermal Property Characterization of Single Crystal Diamond With Varying Isotopic Composition,* Ph.D., Wayne State University, Detroit, MI, 1993.
31. D. P. H. Hasselman, J. Composite Mater. **12**, 403–407 (1978).
32. B. R. Lawn, N. P. Padture, F. Guiberteau, and H. Cai, Acta Metall. **42**, 1683–1693 (1994).
33. J. T. Hagan and M. V. Swain, J. Physics: D **11**, 2091–2102 (1978).
34. R. H. J. Hannink and M. V. Swain, J. Mater. Sci. **16**, 1428–1431 (1981).
35. D. B. Marshall and M. V. Swain, J. Am. Ceram. Soc. **71**, 399–407 (1988).
36. J. Lankford, J. Am. Ceram. Soc. **66**, C212–213 (1983).
37. N. P. Padture, J. Am. Ceram. Soc. **77**, 519–523 (1994).
38. B. C. Muddle and P. M. Kelly, Materials Forum **11**, 182–193 (1988).
39. I-W. Chen, J. Am. Ceram. Soc. **69**, 189–194 (1986).
40. B. R. Lawn, J. Am. Ceram. Soc. **66**, 83–91 (1983).
41. L. Ewart and S. Suresh, J. Mater. Sci. **22**, 1173–1192 (1987).
42. S. Suresh and J. R. Brockenbrough, Acta Metall. **36**, 1455–1470 (1988).
43. S. Suresh, *Fatigue of Materials* (Cambridge University Press, Cambridge, 1991).
44. N. P. Padture and B. R. Lawn, Acta Metall. **43**, 1609–1617 (1995).
45. B. R. Lawn, B. J. Hockey, and S. M. Wiederhorn, J. Mater. Sci. **15**, 1207–1223 (1980).

J. Mater. Res., Vol. 10, No. 10, Oct 1995

2625